IOP Publishing | Institute of Physics and Engineering in Medicine Physics in Medicine & Biology

Phys. Med. Biol. **61** (2016) 2582–2593 doi:10.1088/0031-9155/61/6/2582

Contactless remote induction of shear waves in soft tissues using a transcranial magnetic stimulation device

Pol Grasland-Mongrain[1], Erika Miller-Jolicoeur[1], An Tang[2,3], Stefan Catheline[4,5] and Guy Cloutier[1,3,6,7]

[1] Laboratory of Biorheology and Medical Ultrasonics, Research Center of the University of Montreal Hospital (CRCHUM), Montreal, QC, Canada
[2] Laboratory of Clinical Image Processing, CRCHUM, Montreal, QC, Canada
[3] Department of Radiology, Radio-Oncology and Nuclear Medicine, University of Montreal, Montreal, QC, Canada
[4] Laboratoire de Thérapie et Applications des Ultrasons, Inserm u1032, Inserm, Lyon, F-69003, France
[5] Université Lyon 1 Claude Bernard, Lyon, F-69003, France
[6] Institute of Biomedical Engineering, Montreal, QC, Canada

E-mail: guy.cloutier@umontreal.ca

Received 23 September 2015, revised 6 January 2016
Accepted for publication 14 January 2016
Published 8 March 2016

Abstract

This study presents the first observation of shear waves induced remotely within soft tissues. It was performed through the combination of a transcranial magnetic stimulation device and a permanent magnet. A physical model based on Maxwell and Navier equations was developed. Experiments were performed on a cryogel phantom and a chicken breast sample. Using an ultrafast ultrasound scanner, shear waves of respective amplitudes of 5 and 0.5 μm were observed. Experimental and numerical results were in good agreement. This study constitutes the framework of an alternative shear wave elastography method.

Keywords: shear wave elastography, Lorentz force, radiation pressure, transcranial magnetic stimulation

(Some figures may appear in colour only in the online journal)

[7] Author to whom any correspondance should be addressed.

1. Introduction

The propagation of elastic waves in solids has been described in various fields of physics, including geophysics, soft matter physics or acoustics. Elastic waves can be separated in two components in a bulk: compression waves, corresponding to a curl-free propagation; and shear waves, corresponding to a divergence-free propagation. Shear waves have drawn a strong interest in medical imaging with the development of shear wave elastography methods (Muthupillai *et al* 1995, Sarvazyan *et al* 1998). These methods use shear waves to measure or map the elastic properties of biological tissues. Shear wave speed measurement permits calculation of the tissue shear modulus. Shear wave elastography techniques have been successfully applied to several organs such as the liver (Sandrin *et al* 2003), the breast (Berg *et al* 2012), the arteries (Schmitt *et al* 2010) and the prostate (Cochlin *et al* 2002), to name a few examples. The brain has also been studied, and its elasticity is of strong interest for clinicians (Kruse *et al* 2008, Mariappan *et al* 2010). For example, it has been shown that Alzeihmer's disease, hydrocephalus or multiple sclerosis are associated with changes in brain elastic properties (Taylor and Miller 2004, Wuerfel *et al* 2010, Murphy *et al* 2011).

Clinical shear wave elastography techniques currently rely on an external vibrator (Muthupillai *et al* 1995, Sandrin *et al* 2003) or on a focused acoustic wave (Sarvazyan *et al* 1998, Nightingale *et al* 2002) as the shear wave source. However, these techniques are limited in situations where the organ of interest is located behind a strongly attenuating medium like the brain behind the skull surrounded by the cerebrospinal fluid. While external shakers are able to transmit shear waves, using acoustic, pneumatic, piezoelectric or electromagnetic actuators (Weaver *et al* 2001, Braun *et al* 2003, Kruse *et al* 2008, Latta *et al* 2011), this approach can be uncomfortable for patients. Alternatively, acoustic waves may be transmitted through the skull to induce shear waves inside the brain, but the skull attenuates and deforms the acoustic beam, preventing efficient transmission of energy (Tanter *et al* 1998). This is nevertheless used in magnetic resonance acoustic radiation force imaging where brain tissue displacement is used to correct acoustic phase aberration during high-intensity focused ultrasound treatment (Hertzberg *et al* 2010, Marsac *et al* 2012). Recently, it has also been shown that physiological body motion can be used, via blood pulsation (Weaver *et al* 2012, Hirsch *et al* 2013) or noise correlation (Gallot *et al* 2011, Zorgani *et al* 2015), but these methods still require further developments before clinical application in the context of brain elastography.

Recently, it was demonstrated that the combination of an electrical current and a magnetic field could create displacements propagating as shear waves in biological tissues (Basford *et al* 2005, Grasland-Mongrain *et al* 2014). If the electrical current is induced using a coil, this would allow the technique to remotely induce shear waves. In the case of brain elastography, this would allow inducing shear waves directly inside the brain.

To achieve this objective, we propose to use a transcranial magnetic stimulation (TMS) device (Hallett 2000). This instrument is used to induce an electrical current directly inside the brain by using an external coil. TMS is currently employed by neurologists to study brain functionality (Ilmoniemi *et al* 1999) and by psychiatrists to treat depression (Sakkas *et al* 2006). TMS is occasionally combined with magnetic resonance imaging (MRI) (Bohning *et al* 1997, Devlin *et al* 2003); however, no study has yet reported the production of shear waves when combining TMS and a magnetic field.

This article first presents the physical model describing the generation of shear waves resulting from the combination of a remotely induced electrical current and a magnetic field. It describes experiments performed in polyvinyl alcohol (PVA) cryogel and biological tissue samples. A numerical study of the experiments is then presented. Results show a good consistency between experimental and numerical displacement maps. Some critical excitation

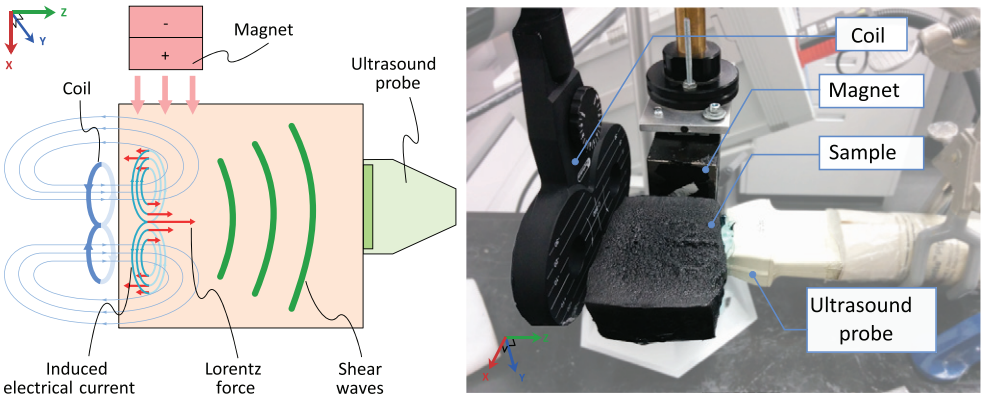

Figure 1. (A) Scheme of the experiment. A coil is inducing remotely an electrical current (blue circles) in a sample. A magnet creates a magnetic field (pink arrows) in the sample. The combination of the electrical current and the magnetic field induces a Lorentz force (red arrows). This force creates displacements which propagate as shear waves (green waves) tracked through an ultrasound probe. (B) Experimental setup. The tested sample is a polyvinyl alcohol tissue-mimicking phantom (the plastic box surrounding the phantom is removed for clarity). The electrical current is applied by the coil. The magnetic field is created by the magnet. Ultrasound images are acquired through the probe coupled to the sample.

parameters were investigated as well as dependence of the shear wave amplitude with the magnetic field and electrical current intensity. Practical implementation in the context of shear wave elastography of the brain is finally discussed.

2. Physical model

We set up the experiment illustrated in figure 1(A). The key components are as follows: a coil induces an electrical current $\mathbf{j}$ in the sample; a magnet creates a magnetic field $\mathbf{B}$; an ultrasound probe tracks displacements $\mathbf{u}$ propagating as shear waves in the sample. X is defined as the main magnetic field axis, Z as the main ultrasound propagation axis, and Y an axis orthogonal to X and Z following the right-hand rule. The origin of coordinates (0,0,0) is located in the middle of the coil (i.e. between the two loops).

For a circular coil centered in (0,0,0) of linear element $\mathrm{d}\mathbf{l}$ crossed by an electrical current $I(t)$, using Coulomb gauge (i.e. $\nabla \cdot \mathbf{A} = 0$ where $\mathbf{A}$ is the magnetic potential vector), and negligible propagation time of electromagnetic waves, the electrical field $\mathbf{E}(\mathbf{r}, t)$ along space $\mathbf{r}$ and time t is equal to (Jackson 1998):

$$\mathbf{E}(\boldsymbol{r}, t) = -\nabla \Phi - \frac{\mathrm{d}I}{\mathrm{d}t} \frac{N\mu_0}{4\pi} \int \frac{\mathrm{d}\boldsymbol{l}}{r} \tag{1}$$

where Φ is the electrostatic scalar potential, N is the number of turns of the coil and μ_0 is the magnetic permeability of the coil material. In an unbounded medium, Φ is only due to free charges (Grandori and Ravazzani 1991), that we supposed negligible in our case. Being additive, the total electrical field created by two or more coils is simply the sum of the contribution of each coil. The induced electrical current density $\mathbf{j}$ is retrieved using the local Ohm's law $\mathbf{j} = \sigma\mathbf{E}$, where σ is the electrical conductivity of the medium.

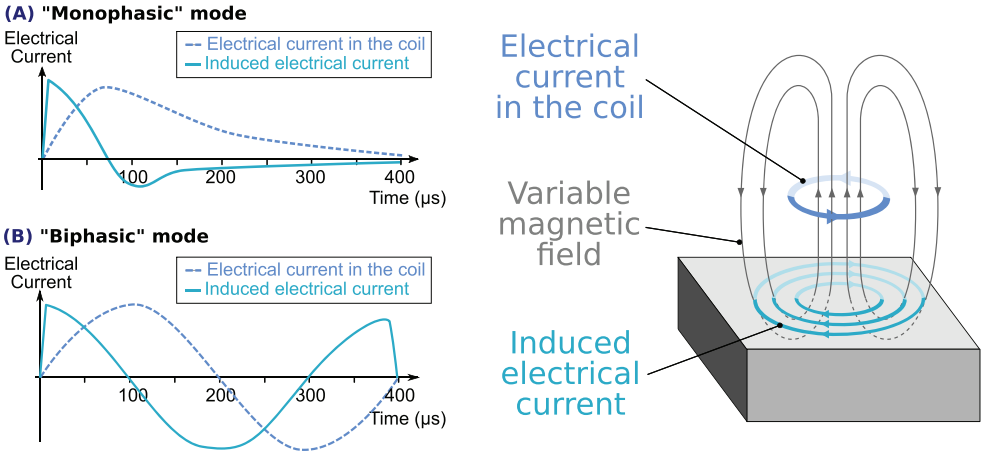

Figure 2. (A) Electrical current in the coil and induced electrical current when used in 'monophasic' mode. (B) Electrical current in the coil and induced electrical current when used in 'biphasic' mode. (Right) Scheme of the induction of electrical current in the medium by the TMS coil.

The body Lorentz force $\mathbf{f}$ can then be calculated using the relationship $\mathbf{f} = \mathbf{j} \times \mathbf{B}$, where $\mathbf{B}$ is the magnetic field created by the permanent magnet. Considering the tissue as an elastic, linear and isotropic solid, Navier's equation governs the displacement $\mathbf{u}$ at each point of the tissue submitted to an external body force $\mathbf{f}$ (Aki and Richards 1980):

$$\rho \frac{\mathrm{d}^2 \boldsymbol{u}}{\mathrm{d}t^2} = \left(K + \frac{4}{3}\mu\right) \nabla (\nabla \cdot \mathbf{u}) + \mu \nabla \times (\nabla \times \mathbf{u}) + \mathbf{f} \tag{2}$$

where ρ is the medium density, $\mathbf{u}$ the local displacement, K the bulk modulus and μ the shear modulus.

Using Helmholtz decomposition $\mathbf{u} = \nabla\varphi + \nabla \times \psi$, where φ and ψ are respectively a scalar and a vector field, two elastic waves can be retrieved: a compression wave, propagating at a celerity $c_\mathrm{k} = \sqrt{(K + \frac{4}{3}\mu)/\rho}$, and a shear wave, propagating at a celerity $c_\mathrm{s} = \sqrt{\mu/\rho}$ (Sarvazyan *et al* 1998). As ρ varies typically by a few percent between different soft tissues (Cobbold 2007), we can suppose an homogeneous density, and measuring c_s allows to compute the shear modulus μ of the tissue.

3. Materials and methods

In the experimental setup, pictured in figure 1(B), the electrical current was induced by a clinical TMS device using a 2 × 75 mm diameter coil (MagPro R100 device with the C-B60 Butterfly coil, MagVenture, Farum, Danemark). The coil was placed 1 cm away from the medium, without any contact, and fixed to an independent support. The electrical current in the coil was in 'monophasic' mode, i.e. a half cycle of 0.4 ms with a rising time of 70 μs, as illustrated in figure 2(A). Alternatively, a 'biphasic' mode, i.e. a full sinus cycle of 0.4 ms, could be used, as illustrated in figure 2(B). According to the specifications of the manufacturer, at 100% amplitude, the current reached a magnitude of 149×10^6 A·s^{-1} in the coil, leading to a peak transient magnetic field of 2 T (i.e. 30 kT·s^{-1} during rising time) at the surface of the coil and of 0.74 T (i.e. 12 kT·s^{-1} during rising time) at 20 mm depth.

The magnetic field was induced by a $5 \times 5 \times 5\,\text{cm}^3$ N48 NdFeB magnet (model BY0Y0Y0, K&J Magnetics, Pipersville, PA, USA). The magnet was placed 1 cm away from the medium, without any contact, and fixed to a second independent support. In the medium location, the magnetic field intensity ranged from 100 to 200 mT, as measured by a gaussmeter (Model GM2, AlphaLab, Salt Lake City, UT, USA).

The main tested sample was a $4 \times 8 \times 8\,\text{cm}^3$ water-based tissue-mimicking phantom made with 5% PVA, 0.1% graphite powder and 5% NaCl, giving a theoretical electrical conductivity of 7.5 $\text{S}\cdot\text{m}^{-1}$. Three freezing/thawing cycles were applied to stiffen the material (Fromageau *et al* 2007). The graphite powder (#282863 product, Sigma-Aldrich, Saint-Louis, MO, USA) was made of submillimeter particles, which presented a speckle pattern on ultrasound images. The sample was placed in a rigid plastic box of 2 mm thick layers with an opening on a side to introduce the ultrasound probe. The rigid box simulated a solid interface such as a skull and also ensured that any observed movement was not due to the surrounding displacement of air. Alternatively, we used a similar phantom made of 5% PVA, 0.1% graphite powder and 2% NaCl, giving a theoretical electrical conductivity of 3.5 $\text{S}\cdot\text{m}^{-1}$. A biological tissue sample was also tested. This tissue was a chicken breast sample of approximately $3 \times 5 \times 5\,\text{cm}^3$ bought in a local grocery. It was degassed in a 20 °C saline water (0.9% NaCl) during two hours prior to the experiment.

Each sample was observed with a 5 MHz ultrasonic probe made of 128 elements (ATL L7-4, Philips, Amsterdam, Netherlands) coupled to a Verasonics scanner (Verasonics V-1, Redmond, WA, USA). The probe was in contact with the sample with an ultrasound coupling gel but was fixed on a third independent support. It was used in ultrafast mode (Bercoff *et al* 2004) to acquire 1000 frames per second using plane waves reconstructed using the Stolt's fk migration algorithm (Garcia *et al* 2013). The Z component of the displacement in the sample was observed by performing cross-correlations between radiofrequency images with a speckle-tracking technique, using 128×5 pixels^2 cross-correlation windows (Montagnon *et al* 2012). Noise was partly reduced using a low-pass frequency filter (cut-off frequency at 1 kHz). Time $t = 0$ ms was defined as the electrical burst emission.

Great care was taken to ensure that the three supports were not in contact and fixed separately. It could ensure that any vibration of one of the element could not be transmitted to the medium.

4. Numerical study

Additionally to the experiments, a 3D simulation was performed using Matlab (Matlab 2010, The MathWorks, Natick, MA, USA). The numerical study was performed by calculating the electrical current induced by the coil, simulating the magnetic field created by the permanent magnet, computing the resulting Lorentz force inside the medium, and finally computing the propagation along space and time of the displacement due to the Lorentz force.

Using equation (1) with two 75 mm diameter coils crossed by a $149 \times 10^6\ \text{A}\cdot\text{s}^{-1}$ electrical current, representing the TMS coil used in the experiment, the electrical field E was calculated in a $20 \times 10 \times 20\,\text{cm}^3$ volume (see Grandori and Ravazzani (1991) for details on mathematical solving). Using Ohm's law, the electrical current $\mathbf{j}$ was estimated assuming an electrical conductivity $\sigma = 7.5\ \text{S}\cdot\text{m}^{-1}$. No border effect has been taken into account. Induced electrical current in a XY plane at a depth of 2 cm with $2 \times 2\,\text{mm}^2$ pixels is illustrated in figure 3(A), with colors indicating the absolute magnitude and arrows the direction. The electrical current reached a density of 4 $\text{kA}\cdot\text{m}^{-2}$ at the medium location.

A finite element software (Finite Element Magnetic Method (Meeker 2006)) was used to produce a 2D simulation of the magnetic field $\mathbf{B}$. The magnetic field was supposed to be

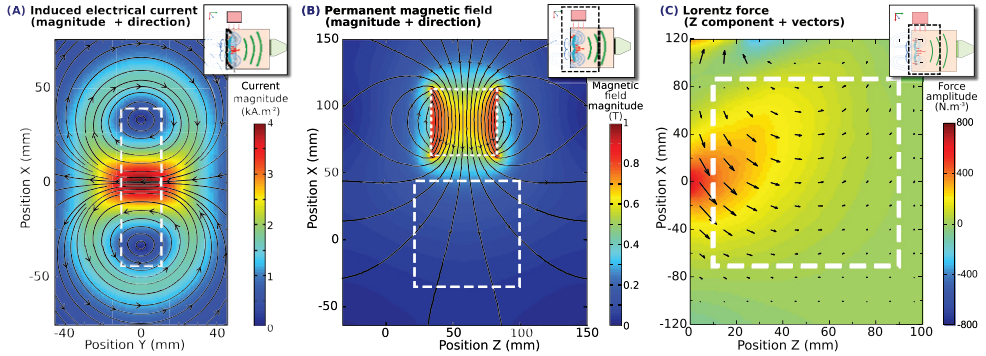

Figure 3. (A) Electrical current induced by two 75 mm-diameter coils, in a *XY* plane in a 7.5 $S{\cdot}m^{-1}$ medium at 2 cm of the coil, as calculated analytically. Black lines are representing the electrical current lines and colors the magnitude. The electrical current reached a magnitude of 4 $kA{\cdot}m^{-2}$ in the medium location (dashed line). (B) Magnetic field as simulated by the Finite Element Magnetic Method software from a $5 \times 5\,cm^2$ NdFeB magnet (dotted line). The magnetic field ranged from 100 to 200 mT at the medium location (dashed line). Black lines are representing the magnetic field lines and colors the magnitude. (C) Lorentz force in a *XZ* plane in the medium, as calculated from the electrical current and the magnetic field. Arrows are representing force vectors and colors the amplitude of the *Z* component. The Lorentz force reached a magnitude of 600 $N{\cdot}m^{-3}$ in the medium location (dashed line).

approximately constant in the sample along the *Y* axis. The magnetostatic problem was solved from equations $\nabla \times H = \nabla \times M$, $\nabla B = 0$ and $B = \mu_p H$, with H the magnetic field intensity, M the magnetization of the medium, B the magnetic flux density, and μ_p the medium permeability. The medium was considered as linear and the space was meshed with approximately $0.5\,cm^2$ triangles. The software simulated a N48 NdFeB permanent magnet of $5 \times 5\,cm^2$ placed in a $30 \times 30\,cm^2$ surface of air. Resulting magnetic field in a *XZ* plane is illustrated in figure 3(B), with colors indicating the absolute magnitude and arrows the direction. The magnetic field ranged from 100 to 200 mT at the medium location.

The body Lorentz force $\mathbf{f}$ was computed from the cross-product of $\mathbf{j}$ and $\mathbf{B}$. The resulting Lorentz force in a *XZ* plane with $2 \times 2\,mm^2$ pixels is illustrated in figure 3(C), with arrows indicating the Lorentz force vector and colors its amplitude along *Z* (as the electrical current is induced in the *XY* plane and the magnetic field essentially along the *X* direction, the Lorentz force is mainly along the *Z* direction). The Lorentz force reached a magnitude of 600 $N{\cdot}m^{-3}$ in the medium location.

Finally, the displacement $\mathbf{u}(\mathbf{r}, t)$ was determined analytically along space (pixels of $2 \times 2\,mm^2$) and time (steps of 1 ms) by solving equation (2) with the Green operator (Grandori and Ravazzani 1991). It used a medium density ρ of 1000 $kg{\cdot}m^{-3}$, a bulk modulus K of 2.3 GPa and a shear modulus μ of 16 kPa, corresponding to a shear wave speed of 4 $m{\cdot}s^{-1}$.

5. Results

Z component maps of the displacements over time are illustrated in figure 4, respectively 1, 2, 4, 8 and 12 ms after current emission, as given by the simulation (A), the experiment in the PVA phantom (B) and the experiment in the chicken breast sample (C). Initial displacements occurred where the Lorentz force had the highest magnitude, on the opposite side of the ultrasound probe, so the displacement is not due to the probe vibration. Displacements reached

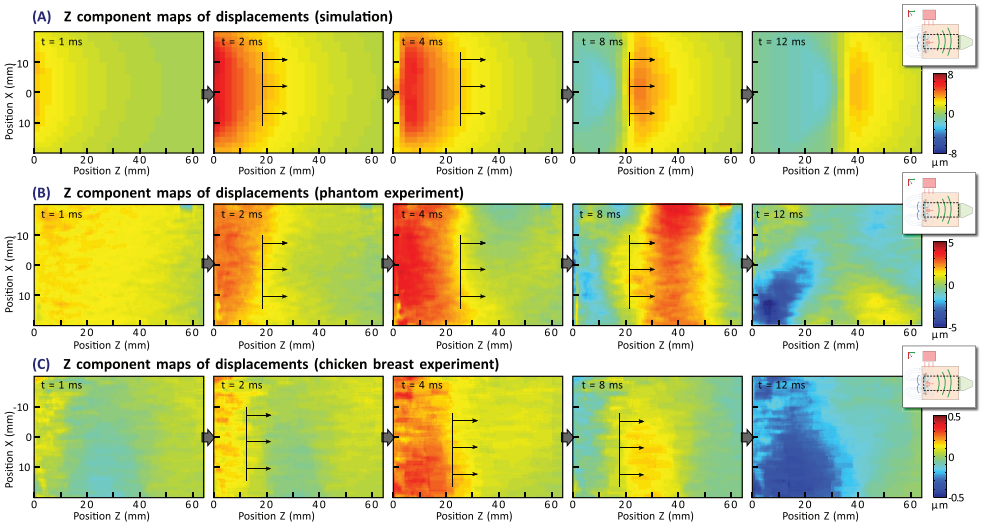

Figure 4. *Z* component maps of the displacement over time, respectively 1, 2, 4, 8 and 12 ms after current emission, as given by the simulation (A), the experiment on the PVA phantom (B) and on the chicken sample (C). A shear wave can be observed in the three cases, with hand drawn black arrows indicating propagation of the wave front.

an amplitude of 5 μm in the phantom and 0.5 μm in the chicken sample. Displacement maps were harder to compute in the chicken breast sample, as electrical conductivity was lower and as speckle was of poorer quality. They propagated as shear waves, whose speed was 4 m·s^{-1} for the simulation, 4.0 $\pm$ 1.0 m·s^{-1} for the PVA phantom and 3.5 $\pm$ 1.0 m·s^{-1} for the chicken sample along the *Z* axis. These values correspond to Young's moduli of 48 $\pm$ 24 kPa for the PVA phantom and 37 $\pm$ 20 kPa for the chicken sample.

Figures 5(A)–(B) illustrates experimental *Z*-component maps 6 ms after excitation, when using the 'monophasic' mode and the 'biphasic' mode, respectively. Average displacements in the region of interest are 3.3 μm in the first case and 0.2 μm in the second case. Only the 'monophasic' mode was able to induce observable shear waves.

Figures 5(C)–(D) depicts experimental *Z*-component maps 6 ms after excitation in a 5% salt medium and in a 2% medium, respectively (note that (A) and (C) are identical and correspond to the same experiment). Average displacements in the region of interest are 3.3 μm in the first case and 1.3 μm in the second case. When the electrical conductivity of the medium decreases, the shear wave amplitude also decreases roughly by a same factor.

Figures 5(E)–(F) presents experimental *Z*-component maps 6 ms after excitation, when selecting 100% and 50% amplitudes in the coil, respectively (as these experiments were conducted in the 5% salt medium, panels (A) and (E) are identical). Average displacements in the region of interest are 3.3 μm in the first case and 1.4 μm in the second case. Notice that the shear wave amplitude is roughly divided by two when the excitation amplitude is halved (according to the device panel).

Finally, figures 5(G)–(H) illustrates *Z*-component maps 6 ms after excitation in a 2% salt medium, when excited with a 100% and a -100% amplitude in the coil, respectively (note that (D) and (G) correspond to the same experiment). Average displacements in the region of interest are 1.3 μm in the first case and -1.4 μm in the second case. As expected, the displacement amplitude is inverted when the excitation is inverted.

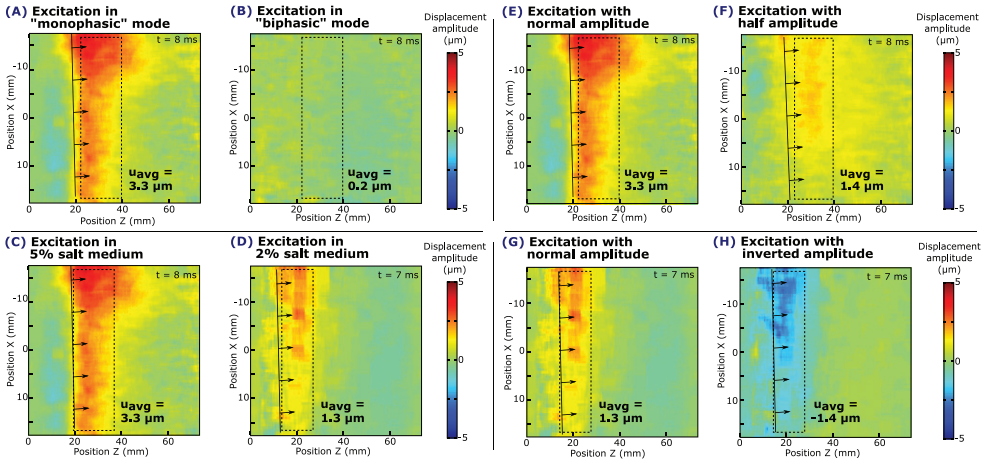

Figure 5. (A)–(B) Z component maps with an excitation in 'monophasic' and 'biphasic' modes, respectively. Shear waves can be observed in 'monophasic' mode, but no displacement occurs in 'biphasic' mode. (C)–(D) Z component maps with a monophasic excitation in 5% and 2% salt media, respectively. The amplitude of displacements is approximately divided by the same factor as the ratio of the electrical conductivity. (E)–(F) *Z* component maps in a 5% saline medium with a monophasic excitation with 100% amplitude and 50% amplitude, respectively. The amplitude of displacements is roughly divided by two when the amplitude of the excitation is halved (according to the device panel). (G)–(H) *Z* component maps with a monophasic excitation in a 2% salt medium with 100% positive and negative amplitudes, respectively. The amplitude of displacements is inverted when the excitation amplitude is inverted.

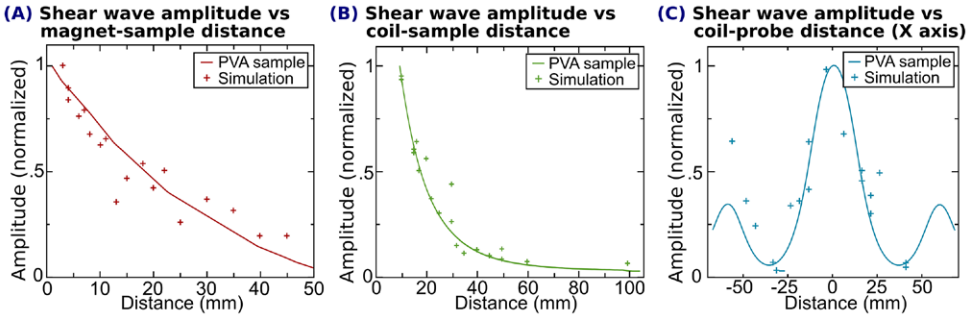

Figure 6. (A) Normalized magnitude of shear waves versus distance along the *X* axis from the magnet: experimental (red markers) and numerical (red line) results. (B) Normalized magnitude of shear waves versus distance along the *Z* axis from the coil: experimental (green markers) and numerical (green line) results. (C) Normalized magnitude of shear waves versus distance along the *X* axis between the center of the coil and the center of the probe: experimental (blue markers) and numerical (blue line) results.

The normalized amplitude of shear waves versus distance between the magnet and the PVA sample was also tested. Results are illustrated in figure 6(A). The effect of the distance between the coil and the PVA sample along the *Z* axis is presented in figure 6(B), whereas that of the distance between the center of the coil and the center of the ultrasound probe along the *X* axis (0 being defined as the coil center aligned with the probe center) is given in figure 6(C).

The amplitude of shear waves was measured as the mean squared displacement between 15 and 25 mm of the coil inside the medium, an arbitrary location where shear waves had high amplitudes. Amplitudes were normalized by the maximum measured, respectively at a distance of 4 mm between the magnet and the sample, 10 mm between the coil and the medium, and 0 mm between the center of coil and the center of probe.

We observed a decrease of the shear wave amplitude when the distance between the medium and the magnet increased, with an excellent agreement between experimental and numerical results. This was expected as the magnetic field decreased with distance. Similar observations can be made when the coil was drawn further from the sample. When we moved the coil along the *X* direction, we observed a strong maximum between two minima separated by 75 mm, corresponding to the length between the two centers of the TMS coil, which is also in agreement with the current density profile along this direction.

6. Discussions

6.1. Practical implementation of the method

This study used an ultrasound device to image the sample and track shear waves as it provides a high temporal resolution and is widely availability. However, for a clinical implementation of the method for brain elasticity imaging, MRI would be more suited as acoustic waves used in ultrasound imaging for shear wave tracking are attenuated by the skull. In a practical MRI implementation using phase sensitive sequences to track shear waves, no additional magnet would be necessary and MRI-compatible TMS coils would need to be used. As most clinical MRI scanners use 1.5 T or higher magnetic fields, which is at least ten times more important than the one used in this study, the displacement amplitude would be increased by a similar factor thus improving shear wave tracking. Magnetic resonance elastography is usually employing continuous shear wave excitations. However, induction of a continuous electrical current in the TMS coil may interfere with MRI measurements, so repetitive triggered transient excitations may be used.

6.2. Displacement amplitude

In the numerical study, the Lorentz force magnitude reached about 600 $N{\cdot}m^{-3}$ for a 150 mT permanent magnetic field and a 7.5 $S{\cdot}m^{-1}$ medium conductivity. The literature provides numerous measurements of grey and white matter electrical conductivity. This parameter is however difficult to measure and thus presents a high variability. It indeed varied from 0.02 to 2 $S{\cdot}m^{-1}$ between measurements (Gabriel *et al* 2009). Using an average value of 0.2 $S{\cdot}m^{-1}$, in a 1.5 T MRI system, the Lorentz force would reach a magnitude of about 160 $N{\cdot}m^{-3}$.

We can compare this magnitude with the acoustic radiation force used for shear wave elastography. This force is calculated with the equation $f_{ARF} = 2\alpha I/c$, where α is the attenuation of the medium, I is the ultrasound intensity, and c is the speed of sound. Using Nightingale *et al* parameters (Nightingale *et al* 2001) ($\alpha = 0.4$ $Np{\cdot}cm^{-1}$, $I = 2.4$ $W{\cdot}cm^{-2}$, and $c = 1540$ $m{\cdot}s^{-1}$), f_{ARF} is about 1200 $N{\cdot}m^{-3}$, which led in their experimental study to displacements on the order of 2.9 μm. The Lorentz force reported in the current study is about one order of magnitude smaller but we could nevertheless observe displacements of 5 μm in the PVA phantom. This may be explained by the fact that it is not only the magnitude of the force, but also the shape and duration of the excitation that contributes to the displacement amplitude.

Note that displacements reached an amplitude of only 0.5 μm in the chicken breast sample. The electrical conductivity of muscles (longitudinal) is about 0.4 $S{\cdot}m^{-1}$ and is expected to decrease notably after animal death (Zheng *et al* 1984). So although the sample was placed in saline water, the effective conductivity can be expected to be quite lower than that of saline (1.8 $S{\cdot}m^{-1}$). This is a probable explanation for the low amplitude of displacements.

As introduced above, the excitation mode and duration also have an influence on the displacement amplitude. For example, the 'biphasic' mode could not induce any observable displacement. This is probably due to the quick succession of positive and negative displacements with a mean at the noise level amplitude.

Finally, one could notice in the numerical study that displacements were slightly higher than the experimental values in the phantom. Various factors like viscosity and border effects, which were not included in our model, could explain this difference. Moreover, there were uncertainties about the electrical current amplitude and shape in the coil, as constructor values were used, and about the electrical conductivity of the medium, as this parameter is not entirely determined by the concentration of NaCl.

6.3. Source localization

In reported experiments, the shear wave source was 3 to 4 cm wide. With currently existing TMS coil geometries, it could hardly be lower than 1 cm. While this is higher than acoustic radiation force using a single point focus (1–2 mm), this last technique is hardly applicable in the brain because of the skull, as mentioned earlier. Compared to current magnetic resonance elastography methods using an external shaker, the shear wave source is far more localized. For whole brain elasticity measurements, having a source spreading on a few cm should not be a problem. For localized measurements with the proposed method, the shear wave source would be placed close to the region of interest, but not inside.

6.4. Safety of the method

Regarding safety issues, strong magnetic fields in MRI systems are considered biologically harmless (Schenck 2000). About the potential harmful effects of the electrical current induced by the coil, safety guidelines based on clinical reports have also been provided for the TMS technique (Rossi *et al* 2009). These guidelines have been respected in the current study: the excitation amplitude stayed within the manufacturer's limits with less than one activation per second (no harmful effect is expected with this configuration). Main concerns would be with repetitive bursts of short repetition periods, as it could increase local temperature in the brain and potentially be detrimental for the instrument. Also, the combination of electrical current induced by the TMS coil with strong magnetic fields can produce displacements in the range of a few tenths of micrometers at most in biological tissues, but no harmful effects have been reported so far with shear waves of this amplitude (Ehman *et al* 2008, Skurczynski *et al* 2009). Precautions linked to the proposed technique are consequently the same as those for TMS and MRI—mainly the absence of ferromagnetic materials in the body.

Acknowledgments

Part of the research has been founded by the Fondation pour la Recherche Médicale, the Natural Sciences and Engineering Research Council of Canada, the Fonds de Recherche du Québec en Santé and the Fondation de l'Association des Radiologistes du Québec. The authors

would like to thank MagVenture and Dr Paul Lespérance of the University of Montreal Hospital for the loan of the TMS devices.

References

Aki K and Richards P G 1980 *Quantitative Seismology* (San Francisco, CA: Freeman)
Basford A T, Basford J R, Kugel J and Ehman R L 2005 Lorentz-force-induced motion in conductive media *Magn. Reson. Imaging* **23** 647–51
Bercoff J, Tanter M and Fink M 2004 Supersonic shear imaging: a new technique for soft tissue elasticity mapping *IEEE Trans. Ultrasonics Ferroelectr. Freq. Control* **51** 396–409
Berg W A *et al* 2012 Shear-wave elastography improves the specificity of breast US: the BE1 multinational study of 939 masses *Radiology* **262** 435–49
Bohning D E, Pecheny A P, Epstein C M, Speer A M, Vincent D J, Dannels W and George M S 1997 Mapping transcranial magnetic stimulation (TMS) fields *in vivo* with MRI *Neuroreport* **8** 2535–8
Braun J, Braun K and Sack I 2003 Electromagnetic actuator for generating variably oriented shear waves in MR elastography *Magn. Reson. Med.* **50** 220–2
Cobbold R S 2007 *Foundations of Biomedical Ultrasound* (New York: Oxford University Press)
Cochlin D L, Ganatra R and Griffiths D 2002 Elastography in the detection of prostatic cancer *Clin. Radiol.* **57** 1014–20
Devlin J, Matthews P and Rushworth M 2003 Semantic processing in the left inferior prefrontal cortex: a combined functional magnetic resonance imaging and transcranial magnetic stimulation study *J. Cogn. Neurosci.* **15** 71–84
Ehman E, Rossman P, Kruse S, Sahakian A and Glaser K 2008 Vibration safety limits for magnetic resonance elastography *Phys. Med. Biol.* **53** 925–35
Fromageau J, Gennisson J L, Schmitt C, Maurice R L, Mongrain R and Cloutier G 2007 Estimation of polyvinyl alcohol cryogel mechanical properties with four ultrasound elastography methods and comparison with gold standard testings *IEEE Trans. Ultrasonics Ferroelectr. Freq. Control* **54** 498–509
Gabriel C, Peyman A and Grant E 2009 Electrical conductivity of tissue at frequencies below 1 MHz *Phys. Med. Biol.* **54** 4863–78
Gallot T, Catheline S, Roux P, Brum J, Benech N and Negreira C 2011 Passive elastography: shear-wave tomography from physiological-noise correlation in soft tissues *IEEE Trans. Ultrasonics Ferroelectr. Freq. Control* **58** 1122–6
Garcia D, Tarnec L, Muth S, Montagnon E, Porée J and Cloutier G 2013 Stolt's f-k migration for plane wave ultrasound imaging *IEEE Trans. Ultrasonics Ferroelectr. Freq. Control* **60** 1853–67
Grandori F and Ravazzani P 1991 Magnetic stimulation of the motor cortex-theoretical considerations *IEEE Trans. Biomed. Eng.* **38** 180–91
Grasland-Mongrain P, Souchon R, Zorgani A, Cartellier F, Chapelon J Y, Lafon C and Catheline S 2014 Imaging of shear waves induced by Lorentz force in soft tissues *Phys. Rev. Lett.* **113** 038101–5
Hallett M 2000 Transcranial magnetic stimulation and the human brain *Nature* **406** 147–50
Hertzberg Y, Volovick A, Zur Y, Medan Y, Vitek S and Navon G 2010 Ultrasound focusing using magnetic resonance acoustic radiation force imaging: application to ultrasound transcranial therapy *Med. Phys.* **37** 2934–42
Hirsch S, Klatt D, Freimann F, Scheel M, Braun J and Sack I 2013 *In vivo* measurement of volumetric strain in the human brain induced by arterial pulsation and harmonic waves *Magn. Reson. Med.* **70** 671–83
Ilmoniemi R J, Ruohonen J and Karhu J 1999 Transcranial magnetic stimulation—a new tool for functional imaging of the brain *Crit. Rev. Biomed. Eng.* **27** 241–84
Jackson J D 1998 *Classical Electrodynamics* 3rd edn (New York: Wiley)
Kruse S A, Rose G H, Glaser K J, Manduca A, Felmlee J P, Jack C R Jr and Ehman R L 2008 Decreased brain stiffness in Alzheimer's disease determined by magnetic resonance elastography *Neuroimage* **39** 231–7
Latta P, Gruwel M, Debergue P, Matwiy B, Sboto-Frankenstein U and Tomanek B 2011 Convertible pneumatic actuator for magnetic resonance elastography of the brain *Magn. Reson. Imaging* **29** 147–52

Mariappan Y K, Glaser K J and Ehman R L 2010 Magnetic resonance elastography: a review *Clin. Anat.* **23** 497–511

Marsac L, Chauvet D, Larrat B, Pernot M, Robert B, Fink M, Boch A L, Aubry J F and Tanter M 2012 MR-guided adaptive focusing of therapeutic ultrasound beams in the human head *Med. Phys.* **39** 1141–9

Meeker D 2006 *Finite Element Method Magnetics* Version 4.2 www.femm.info

Montagnon E, Hissoiny S, Després P and Cloutier G 2012 Real-time processing in dynamic ultrasound elastography: a GPU-based implementation using CUDA *11th Int. Conf. on Information Science, Signal Processing and their Applications (ISSPA)* (Piscataway, NJ: IEEE) pp 472–477

Murphy M, Huston J, Jack C, Glaser K, Manduca A, Felmlee J and Ehman R 2011 Decreased brain stiffness in Alzheimer's disease determined by magnetic resonance elastography *J. Magn. Reson. Imaging* **34** 494–8

Muthupillai R, Lomas D, Rossman P, Greenleaf J, Manduca A and Ehman R 1995 Magnetic resonance elastography by direct visualization of propagating acoustic strain waves *Science* **269** 1854–7

Nightingale K R, Palmeri M L, Nightingale R W and Trahey G E 2001 On the feasibility of remote palpation using acoustic radiation force *J. Acoust. Soc. Am.* **110** 625–34

Nightingale K, Soo M S, Nightingale R and Trahey G 2002 Acoustic radiation force impulse imaging: *in vivo* demonstration of clinical feasibility *Ultrasound Med. Biol.* **28** 227–35

Rossi S, Hallett M, Rossini P M and Pascual-Leone A 2009 Safety, ethical considerations, and application guidelines for the use of transcranial magnetic stimulation in clinical practice and research *Clin. Neurophysiol.* **120** 2008–39

Sakkas P, Psarros C, Papadimitriou G N, Theleritis C G and Soldatos C R 2006 Repetitive transcranial magnetic stimulation (rTMS) in a patient suffering from comorbid depression and panic disorder following a myocardial infarction *Prog. Neuro-Psychopharmacol. Biol. Psychiatry* **30** 960–2

Sandrin L *et al* 2003 Transient elastography: a new noninvasive method for assessment of hepatic fibrosis *Ultrasound Med. Biol.* **29** 1705–13

Sarvazyan A P, Rudenko O V, Swanson S D, Fowlkes J B and Emelianov S Y 1998 Shear wave elasticity imaging: a new ultrasonic technology of medical diagnostics *Ultrasound Med. Biol.* **24** 1419–35

Schenck J F 2000 Safety of strong, static magnetic fields *J. Magn. Reson. Imaging* **12** 2–19

Schmitt C, Hadj Henni A and Cloutier G 2010 Ultrasound dynamic micro-elastography applied to the viscoelastic characterization of soft tissues and arterial walls *Ultrasound Med. Biol.* **36** 1492–503

Skurczynski M, Duck F, Shipley J, Bamber J and Melodelima D 2009 Evaluation of experimental methods for assessing safety for ultrasound radiation force elastography *Br. J. Radiol.* **82** 666–74

Tanter M, Thomas J L and Fink M 1998 Focusing and steering through absorbing and aberrating layers: application to ultrasonic propagation through the skull *J. Acoust. Soc. Am.* **103** 2403–10

Taylor Z and Miller K 2004 Reassessment of brain elasticity for analysis of biomechanisms of hydrocephalus *J. Biomech.* **37** 1263–9

Weaver J B, Pattison A J, McGarry M D, Perreard I M, Swienckowski J G, Eskey C J, Lollis S S and Paulsen K D 2012 Brain mechanical property measurement using MRE with intrinsic activation *Phys. Med. Biol.* **57** 7275–87

Weaver J, Van H E, Miga M, Kennedy F and Paulsen K 2001 Magnetic resonance elastography using 3D gradient echo measurements of steady-state motion *Med. Phys.* **28** 1620–8

Wuerfel J, Paul F, Beierbach B, Hamhaber U, Klatt D, Papazoglou S, Zipp F, Martus P, Braun J and Sack I 2010 MR-elastography reveals degradation of tissue integrity in multiple sclerosis *Neuroimage* **49** 2520–5

Zheng E, Shao S and Webster J G 1984 Impedance of skeletal muscle from 1 Hz to 1 MHz *IEEE Trans. Biomed. Eng.* **31** 477–81

Zorgani A, Souchon R, Dinh A H, Chapelon J Y, Ménager J M, Lounis S, Rouvière O and Catheline S 2015 Brain palpation from physiological vibrations using MRI *Proc. Natl Acad. Sci.* **112** 12917–21